1 **Title: Length control emerges from cytoskeletal network geometry**

2 **Authors:** Shane G. McInally[1], Alexander J.B. Reading[3], Aldric Rosario[2], Predrag R. Jelenkovic[4], Bruce L.
3 Goode[3*], and Jane Kondev[2*]

4 **Affiliations:**

5 [1] Department of Biology and Biotechnology, Worcester Polytechnic Institute, Worcester, MA, 01609, USA.

6 [2] Department of Physics, Brandeis University, Waltham, MA, 02454, USA.

7 [3] Department of Biology, Brandeis University, Waltham, MA, 02454, USA.

8 [4] Department of Electrical Engineering, Columbia University, New York, NY 10027

9 * Correspondence: kondev@brandeis.edu, goode@brandeis.edu

10 **Competing Interest Statement:** Authors declare no competing interests.

11 **Classification:** Biological sciences – Cell biology

12 **Keywords:** Cytoskeleton, Size control, Biological scaling, Emergence

13 **This PDF file includes:**

14   Main Text

15   Figures 1 to 4

16   Supplemental text

17   Supplemental figures 1 to 3

18   Supplemental Table 1

19 **Abstract:** Many cytoskeletal networks consist of individual filaments that are organized into elaborate
20 higher order structures. While it is appreciated that the size and architecture of these networks are critical
21 for their biological functions, much of the work investigating control over their assembly has focused on
22 mechanisms that regulate the turnover of individual filaments through size-dependent feedback. Here,
23 we propose a very different, feedback-independent mechanism to explain how yeast cells control the
24 length of their actin cables. Our findings, supported by quantitative cell imaging and mathematical
25 modeling, indicate that actin cable length control is an emergent property that arises from the cross-linked
26 and bundled organization of the filaments within the cable. Using this model, we further dissect the
27 mechanisms that allow cables to grow longer in larger cells, and propose that cell length-dependent
28 tuning of formin activity allows cells to scale cable length with cell length. This mechanism is a significant
29 departure from prior models of cytoskeletal filament length control and presents a new paradigm to
30 consider how cells control the size, shape, and dynamics of higher order cytoskeletal structures.

31 **Significance Statement:** Cells control the sizes of their cytoskeletal networks to ensure that these
32 structures can efficiently perform their cellular functions. Until now, this ability has been attributed to
33 molecular feedback mechanisms that control the rates at which individual filaments are assembled and
34 disassembled. We find that size control of cytoskeletal networks does not require this type of feedback
35 and can instead be encoded through the physical arrangement of the filaments within that network. These
36 findings have important implications for understanding how the underlying geometry of higher order
37 cytoskeletal networks contributes to cellular control over these structures.

38   **Introduction:** Cells possess the remarkable ability to control the size, shape, and dynamics of their
39   intracellular parts (1–3). This behavior is important for promoting proper organelle function and has been
40   observed for many membrane-bound and cytoskeletal organelles found in diverse eukaryotic cells.
41   Further, it suggests that the ability of a cell to govern the geometric properties of its intracellular
42   structures is a fundamental property of living systems.

43   Cytoskeletal filaments are popular and convenient models used to study the mechanisms that control the
44   size of intracellular structures because their size can be represented by a single dimension, their length.
45   Regardless of their molecular composition (e.g., actin or tubulin), these polymers grow by the addition of
46   molecular building blocks and shrink by their removal. Thus, experimental and theoretical studies of
47   length control aim to identify the nature of the feedback that controls the rates of subunit addition and
48   removal, which allows these filaments to be assembled and maintained at a steady-state length (4).
49   Different mechanisms have been proposed to explain how cytoskeletal structures (e.g., mitotic spindles,
50   cilia, and actin cables) are assembled and maintained at defined lengths, including: limiting-pool models,
51   balance-point models, molecular rulers, antenna models, and concentration gradients (5–10). While each
52   of these mechanisms involves distinct molecular details, they all require a control mechanism that tunes
53   either the assembly rate, the disassembly rate, or both rates in a length-dependent manner. While this
54   level of abstraction is suitable for individual cytoskeletal filaments, it is unclear how well these types of
55   models explain size control of the many higher order cytoskeletal structures found in cells, which have
56   elaborate filamentous architectures, such as cilia/flagella, stereocilia, lamellipodia, and filopodia.

57   Cytoskeletal networks found in nature are typically composed of many individual filaments that are
58   organized into higher order structures. The specific architectures of these larger, composite structures are
59   crucial for their biological functions (e.g., in phagocytosis, cell motility, and pathogenesis), yet much of
60   the work investigating how these structures are assembled and regulated has focused on the mechanisms
61   that control the turnover of individual filaments. To gain a better understanding of how these higher order
62   structures are controlled by the cell, we need to consider the architecture and geometry of these
63   structures and how the arrangement of filaments within these structures contributes to emergent
64   properties of these higher order networks.

65   Here, we address this question using yeast actin cables as a model. Each actin cable in a yeast cell is a
66   bundle comprised of many short, overlapping actin filaments polymerized by formins (11). In the budding
67   yeast *S. cerevisiae*, cables are assembled by two genetically redundant formins, which localize during bud
68   growth to the bud tip (Bni1) and bud neck (Bnr1) (12–14). The cables polymerized by Bni1 and Bnr1 are
69   polarized structures, with their barbed ends oriented toward the bud tip and neck, respectively. This
70   property enables them to serve as railways for essential myosin-based transport of secretory vesicles and
71   organelles to the growing bud cell (11, 15). It is thought that controlling actin cable length promotes
72   efficient intracellular transport and therefore polarized growth in these cells (9, 16–18). In support of this
73   hypothesis, we have recently shown that yeast actin cables grow so that their length closely matches the
74   length of the mother cell in which they are assembled (19). We found that the scaling of cable length with
75   cell length is conferred through control over their assembly - initially cables grow fast, but as they grow
76   longer and approach the back of the cell their rate of growth steadily slows down, or decelerates.
77   Ultimately, cable growth stops when the length of the cable matches the length of the cell. In addition,
78   we showed that this cable deceleration behavior was different in smaller versus larger cells. This suggests
79   that cable growth is tuned in a cell length-dependent manner, but the underlying mechanism has
80   remained unclear.

81   Here, we present a new mathematical model of cable length control that explores how the specific
82   geometry and architecture of a cable can enable length control. This model for cytoskeletal length control

83   is a significant departure from previous length control models because there is no length-dependent
84   molecular feedback mechanism that tunes the rates of assembly or disassembly. Instead, the control over
85   cable length naturally emerges from the geometric arrangement of the filaments within the network.

86   **Results:**

87   **Actin cables undergo length-dependent tapering**

88   To date, actin cables have been thought of as one-dimensional, linear structures (9, 18, 19). Therefore,
89   prior length control studies have treated the cable as having a single barbed end at which actin monomers
90   are added, and a single pointed end at which actin monomers are removed. However, it has been shown
91   that cables are composed of many shorter, overlapping actin filaments bundled together by actin

92   crosslinkers (20). Therefore, we were
93   interested in determining whether the
94   architecture of the cable could provide
95   insights into how its length is controlled (21–
96   23).

97   We started by asking whether the width of
98   cables is uniform along their lengths. To
99   address this, we fixed and stained wildtype
100   haploid budding yeast cells with fluorescently
101   labelled phalloidin and imaged them using
102   super-resolution microscopy. From these
103   images, we traced the entire length of the
104   cables that could be clearly tracked in mother
105   cells (i.e., those that do not intersect with
106   other cables or actin patches) from their origin
107   at the bud neck to their terminal end in the
108   mother cell (Figure 1A). We measured the
109   fluorescence intensity along the entire length
110   of the cable, and took this to be proportional
111   to cable density or thickness. We found that
112   the density of F-actin in cables was not
113   uniform, but instead tapers as cables get
114   longer (Figure 1B). Specifically, F-actin density
115   was greatest in the region closest to the bud
116   neck, where formin-mediated cable assembly
117   takes place, and progressively decreased with
118   cable length. Further, the cable thickness
119   profile was well fit by a single exponential with
120   a decay length of 1.54±0.08 μm (all reported
121   values represent mean ± 95% CI, unless
122   otherwise indicated).

123   **Two-dimensional model of cable length**
124   **control**

125   The tapering of F-actin density we observed in
126   actin cables was reminiscent of tapering
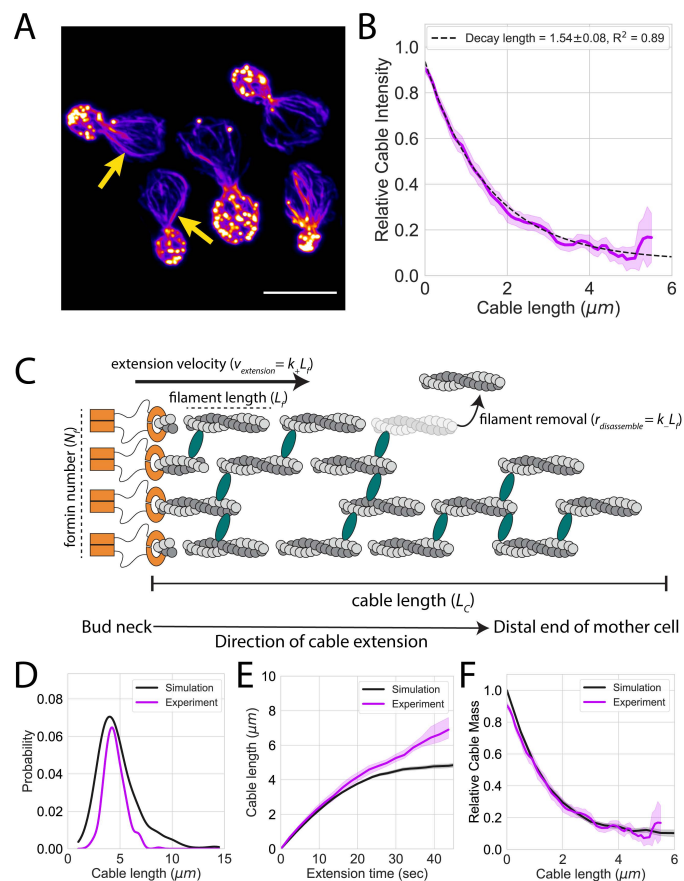
Figure 1: Two-dimensional model of cable length control. (A) Representative maximum intensity projection images of haploid yeast cells fixed and stained with labeled-phalloidin. Arrows indicate single actin cables that clearly display their tapered shape. Scale bar, 5μm. (B) Relative actin cable fluorescence intensity measured in three independent experiments. Solid magenta line and shading, mean and 95% confidence interval for all three experiments (n=47 cables). Tapering profile decay length (±95% CI) was determined by fitting the profile to a single exponential. (C) Schematic of the two-dimensional model of actin cable length control. Multiple formins (orange, N_f) simultaneously assemble short actin filaments with a characteristic length (L_f) at a constant rate (k_+). These filaments are crosslinked and bundled (green ellipses) with neighboring filaments to form the cable and continue to extend into the cell at the same rate at which filaments are assembled by formins ($v_{extension} = k_+ L_f$). Each filament has an independent probability of being targeted for removal ($r_{disassemble} = k_- L_f$) from the cable. Thus, the length of the cable (L_c) is the distance from the site of assembly to the distal tip of the longest surviving filament in the cable. (D-F) Results obtained from simulations (solid black lines) compared with experimental measurements of cable length (D), cable extension rate (E), and cable tapering (F). The parameters used for these 1,000 independent simulations were, $k_+ = 0.50$ sec-1, $k_- = 0.16$ sec-1, $L_f = 500$nm, $N_f = 4$ formins. Solid lines and shading indicate mean and 95% confidence interval, respectively.

127 previously reported for other types of actin networks (e.g., *Listeria* comet tails and fish keratocyte
128 lamellipodial fragments) (24–26). This prompted us to consider whether related mechanisms may explain
129 how the structure and length of actin cables are regulated. To test this idea, we developed a mathematical
130 model of cable length control (Figure 1C), in which multiple formin molecules (N_f) are localized at the bud
131 neck and produce actin filaments of a fixed length (L_f) at a constant rate (k_+). As these filaments are
132 assembled, they are incorporated into the cable bundle by crosslinkers. As a result of polymerization and
133 crosslinking, the entire bundle collectively grows as a single unit, extending into the mother cell at a
134 constant velocity ($v_{extension} = k_+ L_f$), which is equivalent to the number of actin monomers that are
135 added to the growing cable the formins at the bud neck. Once incorporated into the growing bundle, each
136 filament has an independent probability of being targeted for removal through an unspecified
137 disassembly mechanism. Because each of these filaments has a fixed length (L_f), the rate at which
138 monomers are removed from the cable is constant ($r_{disassemble} = k_- L_f$). Thus, the entire length of a
139 cable (L_c) is equal to the distance between its site of assembly (the bud neck) and its distal end, defined
140 by the last surviving filament within the bundle. Importantly, none of these parameters have an inherent
141 length dependence, and therefore all parameters in this model are constants.

142 To derive estimates for the parameters in our model, we referred to our prior study of cable length control
143 (19), in which we determined that the average length of cables in haploid budding yeast was $4.48 \pm$
144 0.98 µm. We also used linear regression to measure the extension velocity of cables (i.e., the slope of the
145 initial linear phase of cable growth) from our prior measurements of cable extension rates in haploid cells
146 ($v_{extension} = 0.25 \pm 0.02$ µm/sec, Supplemental Figure 1A). To estimate the remaining unmeasured
147 parameters in our model, we used the following mathematical relationship that describes the mean length
148 of a bundle of filaments:

$$149 \qquad <L_c> = \lambda \left(\gamma + \ln \left(\frac{k_+}{k_-} N_f \right) \right) \qquad (1)$$

150 where $<L_c>$ is the mean cable length, $\gamma \approx 0.577$ (i.e., the Euler-Mascheroni constant), and N_f is the
151 number of formins assembling a single actin cable; for derivation see Supplemental Text. Importantly, λ
152 is the cable tapering profile in Figure 1B, and can be related to the model parameters through the
153 thickness decay constant, defined as:

$$154 \qquad \lambda = \frac{k_+}{k_-} L_f \qquad (2)$$

155 Using Equation 2 with our measurements of the extension velocity ($v_{extension}$) and the tapering decay
156 profile (λ) we estimate $k_- = 0.16 \pm 0.01$ sec^{-1} (mean ± SD).

157 While we were unable to compute N_f and L_f without direct measurements of at least one of these
158 parameters, a prior electron microscopy study of actin cables in *S. pombe* found that the average length
159 of these filaments was 0.49 ± 0.26 µm (mean ± SD) (20). We used these measurements to estimate
160 $L_f \sim 0.5$µm and, with Equation 1, estimate that four formins ($N_f \sim 4$ formins) cooperate to assemble a
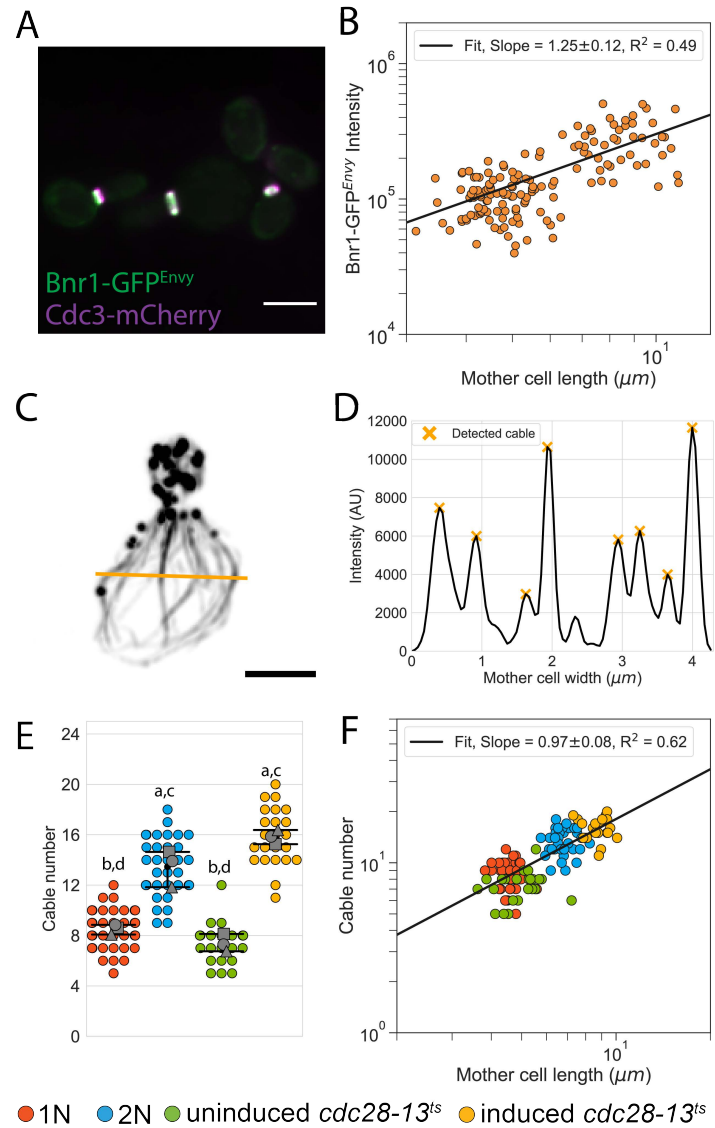161 single cable. Importantly, rewriting Equation 1 using Equation 2 as:

$$162 \qquad <L_c> = \lambda \left(\gamma + \ln \left(\frac{\lambda}{L_f} N_f \right) \right) \qquad (3)$$

163 shows that mean cable length depends on the ratio of the number of formins to filament length (i.e.
164 N_f / L_f), indicating that other values for these parameters can generate cables with the same average
165 length when λ is held constant (Supplemental Figure 2A).

166 Next, we conducted computational
167 simulations using the parameters
168 estimated above $(k_+ = 0.50 \text{ sec}^{-1}$,
169 $k_- = 0.16 \text{ sec}^{-1}$, $L_f = 500$nm, $N_f =$
170 4 formins) and found that this model can
171 assemble actin cables that resemble
172 those observed in vivo. Remarkably, our
173 model produced cables that exhibit a
174 peaked distribution of lengths,
175 decelerated growth, and tapered actin
176 density profiles (Figure 1D-F, black lines),
177 despite the absence of any length-
178 dependent parameters. Next, we directly
179 compared the results of these simulations
180 with our experimental measurements
181 (Figure 1D-F, magenta lines) and found
182 that this model can adequately
183 recapitulate our experimental data
184 without the use of any fitted parameters.
185 We further validated our simulations by
186 comparing these results with the
187 analytical solutions for these cable
188 behaviors (Supplemental Figure 2B-D).

189 **Cable extension velocity is independent**
190 **of cell size**

191 Next, we wanted to determine which
192 parameters in our model may be tuned in
193 a cell length-dependent manner to permit
194 the previously observed scaling of cable
195 length with cell length (19). First, we
196 considered whether the extension
197 velocity may be cell length dependent. To
198 determine how extension velocity
199 changes as a function of cell size we
200 referred to our prior quantification of
201 cable extension rates from temperature-
202 sensitive *cdc28-13ts* cells. At the
203 permissive temperature, *cdc28-13ts* cells
204 are similar in size to wildtype haploid
205 budding yeast; however, their size
206 increases when grown at the non-
207 permissive temperature (19, 27, 28). In
208 our prior study, we quantified cable

Figure 2: The amount of Bnr1 formin at the bud neck and the number of actin cables in a cell scale with cell length. (A) Representative maximum intensity projection image of cdc28-13ts cells grown to different sizes while expressing fluorescently labeled Bnr1 (Bnr1-GFPEnvy) and Cdc3 (Cdc3-mCherry). Scale bar, 5µm. (B) Amount of Bnr1-GFPEnvy localized to the bud neck of cdc28-13ts cells grown to different sizes plotted against mother cell length on a double logarithmic plot and fit using the power-law. Bnr1-GFPEnvy was measured in three independent experiments (n=148 cells). (C) Representative maximum intensity projection images of a haploid yeast cell fixed and stained with labeled-phalloidin. Scale bar, 2µm. Yellow bar indicates the ROI position used to generate the line scan profile (D) used for automated peak detection (orange X's indicate detected actin cables). (E) The number of actin cables measured from haploid (red), diploid (blue), uninduced cdc28-13ts (green), and induced cdc28-13ts (yellow) cells fixed and stained with labeled-phalloidin. Each data point represents an individual cell. Larger symbols represent the mean from each of the three independent experiments (n=119 cells). Error bars indicate 95% confidence intervals. Statistical significance determined by students t-test. Significant differences (p≤0.05) indicated for comparisons with haploid ('a'), diploid ('b'), uninduced cdc28-13ts ('c'), and induced cdc28-13ts ('d'). (F) Actin cable number plotted against mother cell length on a double logarithmic plot and fit using the power-law.

209 extension rates from these enlarged cells by tracking the tips of cables marked with the fluorescent cable
210 reporter Abp140-GFP^Envy. Here, we reanalyzed these measurements by using linear regression to compare
211 the extension velocity (i.e., the slope of the initial linear phase of actin cable growth) in induced and

212   uninduced *cdc28-13^{ts}* cells. We found that despite the nearly 2-fold difference in cell length, the initial
213   extension velocity was not significantly different ($v_{extension,\ uninduced} = 0.22 \pm 0.02$ μm/sec,
214     $v_{extension,\ induced} = 0.24 \pm 0.02$ μm/sec; p = 0.23)(Supplemental Figure 1B). Thus, cable initial
215   extension velocity is independent of cell size and does not likely contribute to the scaling of cable length
216   with cell length.

The amount of formin at the bud neck scales with cell length

218   Next, we considered whether differences in the density or organization of formin molecules at the bud
219   neck (Bnr1) might contribute to the scaling of cable length with cell length. To determine whether the
220   amount of Bnr1 at the bud neck changes in cells of different size, we differentially tagged Bnr1 with GFP^Envy
221   and Cdc3 (a component of the septin collar at the bud neck) with mCherry in *cdc28-13^{ts}* cells (Figure 2A).
222   We grew the cells for either 0, 4, or 8 hours at the non-permissive temperature to induce different changes
223   in cell size, and then returned cells to the permissive temperature to allow polarized growth for one hour.
224   Next, we mixed approximately equal numbers of cells of the three different sizes and performed live
225   imaging on the cell populations using spinning disk confocal microscopy. We used the Cdc3-mCherry
226   channel to generate segmentation masks of the bud neck, and within this mask measured the total
227   fluorescence intensity of Bnr1-GFP^Envy at the bud neck. From the same images, we also measured the
228   distance from the bud neck to the rear of the mother cell.

229   To determine whether the amount of Bnr1-GFP^Envy at the bud neck changes as a function of cell length,
230   we analyzed the data on a double logarithmic plot, which revealed a linear scaling relation between the
231   amount of Bnr1 at the bud neck and cell length (Figure 2B). To determine the nature of this scaling
232   relation, we fit the data using the power law ($y = Ax^{a}$), where a is the scaling exponent that describes
233   the relationship between the two measured quantities, cell length and cable number (3). We found that
234   the scaling exponent was slightly hyperallometric ($a_{formin} = 1.25 \pm 0.11, R^2 = 0.49$), indicating that a
235   greater amount of formin localized to the bud neck in larger cells compared to smaller cells.

The number of actin cables in the mother cell scales with cell length

237   Our observations above prompted us to next ask whether larger cells, which have higher levels of Bnr1 at
238   the bud neck, might assemble thicker cables and/or an increased number of cables. To quantify the
239   number of cables in the mother cell compartment of cells of different size, we used line scans drawn
240   across the equator of haploid, diploid, and *cdc28-13^{ts}* temperature-sensitive cells fixed and stained with
241   fluorescently labelled phalloidin (Figure 2C). Diploid yeast cells have ~2-fold increase in volume compared
242   to haploid cells, and *cdc28-13^{ts}* cells grown at the non-permissive temperature for eight hours have a ~5-
243   fold increase in cell volume (19, 29). Next, we used automated fluorescent peak detection from the line
244   scans to quantify the number of cables in the mother cell compartment (Figure 2D). We also measured
245   the length of the mother cell (i.e., the distance from the bud neck to the rear of the mother cell) in each
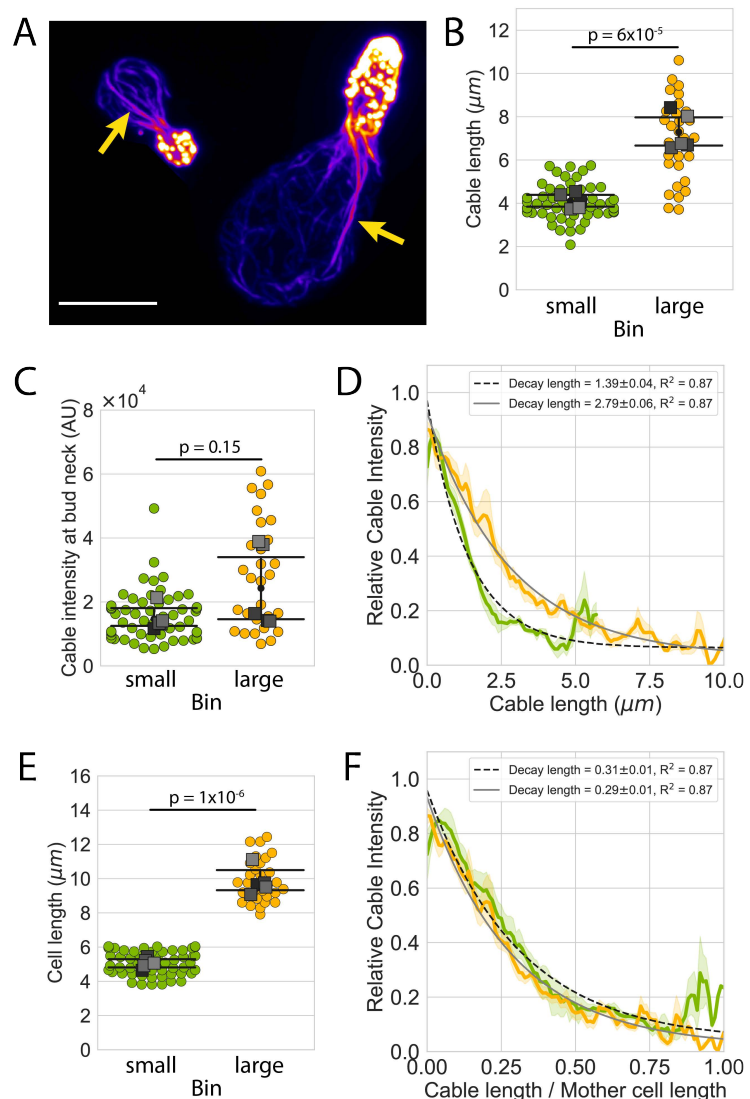246   cell.

247   We found that the mean number of cables was 9 ± 2 in haploid cells and 13 ± 3 in diploid cells. Additionally,
248   the mean number of cables in *cdc28-13^{ts}* cells grown at the permissive temperature was 7 ± 2, while the
249   mean number of cables in *cdc28-13^{ts}* cells grown at the restrictive temperature was 16 ± 3 (Figure 2E). We
250   performed a power law analysis to compare how the number of cables changes as a function of cell size,
251   and found that there is an isometric scaling relation ($a_{cable\ number} = 0.97 \pm 0.07, R^2 = 0.62$) between
252   the number of cables and the length of the cell (Figure 2F).

Actin cables taper in a cell length-dependent manner

254 Thus far, our data suggest that larger
255 cells have higher levels of formin
256 molecules at the site of cable assembly;
257 however, instead utilizing these
258 increased levels of formins to assemble
259 thicker cables, they assemble more
260 cables. To explicitly test whether cables
261 are thicker in larger cells compared to
262 smaller cells, we compared cable
263 tapering profiles from uninduced and
264 induced $cdc28\text{-}13^{ts}$ cells, which were
265 fixed and stained with fluorescently
266 labelled phalloidin. To control for
267 possible differences in staining
268 efficiency, we mixed approximately
269 equivalent amounts of uninduced and
270 induced $cdc28\text{-}13^{ts}$ cells and then
271 simultaneously fixed, stained, and
272 imaged them using super-resolution
273 microscopy (Figure 3A). For each cell in
274 the population, we measured the
275 fluorescence intensity along the length
276 of its cables and the length of the
277 mother cell. To distinguish between the
278 uninduced and induced $cdc28\text{-}13^{ts}$ cells,
279 we used mother cell length to sort cells
280 into bins containing either 'small' or
281 'large' cells. To validate this binning
282 strategy, we plotted the cable lengths
283 we measured from these cells and found
284 that the mean cable length in each bin
285 was consistent with our previous
286 measurements ($L_{cable,\ small} = 4.1 \pm$
287 $0.3\mu m$, $L_{cable,\ large} = 7.3 \pm 0.8\mu m$)
288 (Figure 3B)(19).

Figure 3: Actin cable tapering is cell length dependent. (A) Representative maximum intensity projection images of small (left) and large (right) cdc28-13ts cells fixed and stained with labeled-phalloidin. Arrows indicate single actin cables that clearly display their tapered shape. Scale bar, 5μm. (B) Actin cable length and (C) actin cable fluorescence intensity in the bud neck region measured from mixed populations of uninduced and induced cdc28-13ts cells. Cells were binned based on cell length (E), small cells are indicated in green while large cells are indicated in yellow. Each data point represents an individual cable. Larger symbols represent the mean from each experiment. Error bars indicate 95% confidence intervals. Statistical significance determined by students t-test. (D) Relative actin cable fluorescence intensity plotted against cable length, and (F) relative actin cable fluorescence intensity plotted against the ratio of cable length/cell length. Solid lines and shading, mean and 95% confidence interval. Tapering profile decay lengths (±95% CI) were determined by fitting each profile to a single exponential. All data were generated from five independent experiments (n=84 cables).

289 We first compared the cable
290 fluorescence intensity at the region
291 closest to the bud neck (i.e., the region
292 where new filaments are added to the
293 cable) and found that there was no
294 statistically significant difference between these bins (Figure 3C). These findings indicate that the number
295 of formins incorporating new actin filaments into a single cable is likely similar in cells of different size,
296 and therefore does not contribute to the scaling of cable length with cell length.

297 We next wanted to determine whether differences in how filaments are removed from the cable bundle
298 may contribute to the scaling of cable length with cell length. To test this, we measured the decay length
299 (λ) from the actin tapering profiles for each bin, as this measurement directly reflects the rates at which

300 filaments are added and removed from the bundle (see Equation 2). Comparing the decay length (λ) from
301 the actin tapering profiles for each bin revealed that the decay length was ~2-fold greater in larger
302 compared to smaller cells ($\lambda_{small} = 1.39 \pm 0.04$ μm, $\lambda_{large} = 2.79 \pm 0.06$ μm) (Figure 3D). We also
303 noted that the ratio of decay lengths between bins was similar to the ratio of average cell length between
304 bins ($L_{cell,\ large}/L_{cell,\ small} = 2.0 \pm 0.3$, $\lambda_{large}/\lambda_{small} = 2.0 \pm 0.1$) (Figure 3E). To determine
305 whether these actin tapering profiles were cell length-dependent, we normalized cable length by the
306 length of the cell in which it was measured and then measured the decay lengths from these normalized
307 profiles. Upon normalization, the actin tapering profiles collapse to a single profile with indistinguishable
308 decay lengths ($\lambda_{norm,\ small} = 0.31 \pm 0.01$, $\lambda_{norm,\ large} = 0.29 \pm 0.01$) (Figure 3F), indicating that the
309 mechanism that confers actin cable
310 tapering is a cell length-dependent
311 process.

312 **Scaling of actin cable length by**
313 **tuning filament length**

314 Our observation that cable tapering
315 profiles depend on cell length
316 presents two possible mechanisms
317 by which cells can scale the length of
318 their cables with cell length: tuning
319 the length of filaments assembled by
320 formins in a cell length-dependent
321 manner (Figure 4A, Model 1), or
322 tuning disassembly in a cell length-
323 dependent manner (Figure 4A,
324 Model 2). To distinguish between
325 these two mechanisms, we
326 conducted computational
327 simulations and compared the
328 simulation results to our
329 experimental quantifications of cable
330 length, extension rate, and tapering
331 in smaller and larger cells.

332 First, we conducted simulations of
333 cable assembly using the parameters
334 we derived above for wildtype
335 haploid cells, and compared these
336 results with simulations where the
337 disassembly rate (k_-) had been
338 scaled by cell length. We found that
339 while the decay profiles from these
340 simulations agree with our
341 experimental observations
342 (Supplemental Figure 4A), this
343 mechanism was not able to
344 recapitulate our other experimental
345 observations. Specifically, the cables
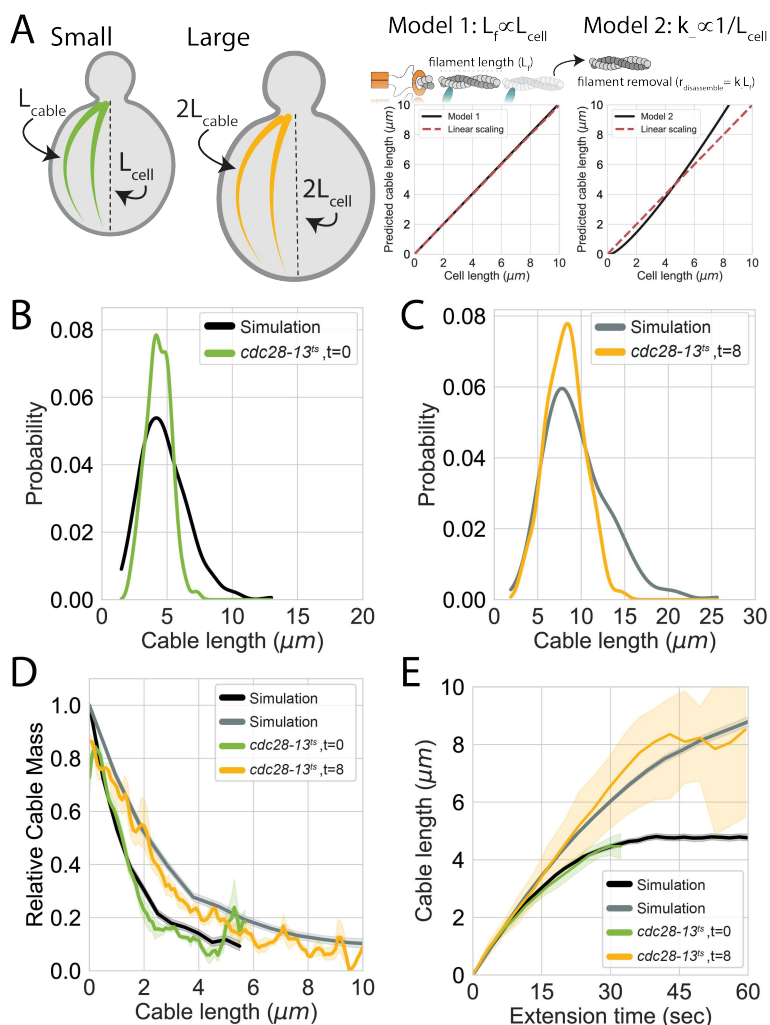
Figure 4: Tuning the length of formin generated filaments scales actin cable length with cell length. (A) Predicted scaling of cable length with cell length when either filament length (Model 1) or disassembly rate (Model 2) is tuned in a cell length dependent manner. Black lines indicate theoretical predictions obtained from Equation 1 where either filament length (left panel) or disassembly rate (right panel) is scaled with cell length. Dashed red lines indicate linear scaling of cable length with cell length. (B-E) Comparisons between simulations conducted using the cell size specific filament lengths (black and grey lines) with experimentally measured actin cable parameters from uninduced (green lines) and induced cdc28-13ts cells (yellow lines). (B-C) Comparisons of actin cable length distributions, (D) actin cable tapering profiles, and (E) actin cable extension rate. Solid lines and shading indicate mean and 95% confidence intervals, respectively.

346   assembled under this mechanism were longer than expected ($< L_c >_{large,simulation} = 11.0 \pm$
347     $1.0 \mu m, < L_c >_{large,experiment} = 8.2 \pm 0.4 \mu m$), and that the ratio of simulated cable lengths was also
348   greater than measured $\left(\frac{<L_c>_{large,\ simulation}}{<L_c>_{small,\ simulation}} = 2.3 \pm 1.9 \right)$ (Supplemental Figure 4B-D). Thus, it appears
349   that tuning the disassembly rate alone cannot explain actin cable length scaling.

350   Next, we wanted to determine whether our experimental observations are consistent with a mechanism
351   where the length of the filaments assembled by formins are scaled with cell length. Importantly, scaling
352   the length of these filaments with cell length requires that both the rates of filament assembly and
353   disassembly are also scaled in a similar manner. This is due to how these rate constants are defined in our
354   model – each rate constant is defined by the amount of time required to either assemble or disassemble
355   a single filament. Therefore, a 2-fold increase in filament length requires twice as much time to assemble
356   that filament and twice as much time to disassemble that filament.

357   We found that our experimental data closely resemble the results of our simulations of cable assembly
358   where the formins assemble filaments whose lengths are scaled with cell length. Specifically, there was
359   no significant difference between mean cable length or the ratio of cable lengths between small and large
360   cells($< L_c >_{large,\ simulation} = 8.7 \pm 0.3 \mu m, < L_c >_{small,\ simulation} = 4.7 \pm 0.2 \mu m;$
361     $\frac{<L_c>_{large,\ simulation}}{<L_c>_{small,\ simulation}} = 1.9 \pm 1.1$; Figure 4B-C) (19). We also found that these simulations closely resemble
362   our measurements of cable tapering (Figure 4D) and cable extension rates measured in small and large
363   *cdc28-13^{ts}* cells (Figure 4E). These findings are further supported by our analytic calculations (Figure 4A
364   for details see Supplemental Text). Thus, our experimental measurements are consistent with a
365   mechanism where actin cable length is scaled to match cell length through a process that tunes the lengths
366   of the filaments assembled by formins, such that formins in longer cells assemble longer filaments.

367   **Discussion**

368   In this study, we present a novel, feedback-independent model of length control that describes how *S.*
369   *cerevisiae* controls and scales the length of its actin cables (Figure 1C). This model differs from prior
370   models of length control in that it does not treat each cable as a one-dimensional filament, nor does it
371   assume that any of the model parameters are tuned in a manner that depends on cable length. Instead,
372   our model considers the actual, two-dimensional arrangement of the cross-linked and bundled filaments
373   that compose the cable (Figure 1C). Additionally, all processes that contribute to the assembly and
374   maintenance of the structure (e.g., the rates of filament addition and removal, the number of nucleators)
375   are treated as constants that are independent of the size of the structure being assembled. Despite the
376   absence of feedback, this model recapitulates all known quantitative features of cable length control
377   when two conditions are met: 1) the filaments that compose cables are bundled, and 2) each filament is
378   removed from the bundle with an independent probability. Thus, rather than relying on size-dependent
379   feedback, control over cable length instead emerges from the geometric arrangement of the shorter
380   filaments that comprise the network.

381   Due to the minimal number of experimentally accessible parameters that define this model, we were able
382   to use our quantitative experimental measurements to generate predictions for each of the parameters
383   in our model, and then test these predictions using computational simulations. We found that our
384   simulations of actin cable assembly using these parameters capture the key quantitative phenotypes
385   displayed by actin cables in vivo – the distribution of cable lengths is peaked, cable extension rate
386   decelerates as the cable grows longer, and cable thickness tapers along their length (Figure 1D-F). While
387   the results of these simulations are very similar to our experimental measurements, we found that there
388   are some notable differences (e.g. the width of the distribution from the simulation is greater than the

389 width of the distribution measured experimentally). These differences between our theoretical and
390 experimental results suggest that while our model adequately describes the mean behavior of cables (e.g.,
391 average cable length, extension rate, etc.) there are likely to be other parameters that further control the
392 assembly and length of actin cables in vivo. Additionally, some of these differences may arise due to the
393 complicated nature of performing quantitative experiments on such a highly dynamic cytoskeletal system.
394 We expect that further technological developments that increase the spatial and temporal resolution with
395 which we can observe actin cables in live cells will help to further refine the predictions for the parameters
396 we identify in this study.

397 We were also interested in testing how the parameters in our model may be tuned in a cell length
398 dependent manner to confer the scaling of actin cable length with cell length. Our prior work provided a
399 quantitative description of how cables grow to lengths that closely match the length of the cell, however,
400 we could only speculate about possible molecular mechanisms that would confer this behavior (19). Here,
401 we were able use our new model of cable length control to computationally and experimentally eliminate
402 potential mechanisms that may confer this scaling behavior.

403 Actin cables are assembled by two complementary sets of formins, one localized to the bud neck (Bnr1)
404 and one localized to the bud tip (Bni1) (12–14). Our study has focused only on the cables assembled by
405 Bnr1, which assembles and organizes cables that enter the mother cell. Prior studies have shown that
406 Bnr1 colocalizes with components of the septin collar in regularly spaced pillars around the bud neck (30–
407 32). These pillars are thought to serve as sites of actin cable assembly, as actin cables have been observed
408 to emerge from these sites as they grow into the mother cell. Additionally, it has been observed that the
409 diameter of the bud neck scales with cell length through an unknown mechanism (33). Therefore, we
410 sought to determine whether these sites of actin cable assembly are sensitive to changes in cell size in
411 order to assemble longer cables in larger cells.

412 Our quantitative analyses of how cables are assembled in cells of different sizes revealed that while there
413 is a greater amount of formin (Bnr1) localized to the bud neck in larger cells (Figure 2B), these cables are
414 assembled at the same rate (Supplemental Figure 1B) and have the same initial thickness as smaller cells
415 (Figure 3B). Additionally, we found that larger cells assemble a greater number of cables when compared
416 with smaller cells (Figure 2E-F). Taken together, these results suggest that the molecular composition and
417 arrangement of formins within these sites of cable assembly are likely cell size independent, but that the
418 number of these assembly sites scales with cell length. It is currently unknown how the size, number, and
419 composition of these cable assembly sites is determined, but we suspect that these features of the actin
420 cable network are important to ensure that the flux of growth factors from the mother cell is sufficient to
421 support the growth of the daughter cell. This hypothesis is supported by the observation that larger
422 mother cells produce larger daughter cells (27, 34), and suggests that actin cables may play an important
423 role in controlling the birth size of daughter cells.

424 Our analysis of actin cable tapering profiles from cells of different sizes presented two possible
425 mechanisms to scale actin cable length with cell length – either the rate at which filaments are removed
426 from the cable, or the length of the filaments that compose the cable are scaled with cell length. When
427 we compared computational simulations and analytic calculations of each mechanism with our
428 experimental measurements, we found that our data are consistent with a mechanism where the length
429 of the filaments that compose the cable are tuned in a cell length dependent manner (Figure 4,
430 Supplemental Text). While we have not generated direct experimental evidence to support this
431 mechanism, prior studies have demonstrated that mutants that lack the ability to properly tune formin
432 activity exhibit defects in actin cable length regulation and organization (16–18, 35, 36). Therefore, we
433 suspect that the tuning of filament length may be driven by regulators that either inhibit formin activity

434 (e.g., Smy1 and Hof1), or displace formins from the barbed ends of growing filaments (e.g., Bud14).
435 Furthermore, it is unclear how the activity or abundance of these types of formin regulators is controlled
436 in a cell length dependent manner. Generally, protein abundance is thought to scale with cell volume,
437 such that their concentration is maintained across variations in cell size (37). However, recent studies have
438 identified subsets of proteins that deviate from this behavior and either 'sub-scale' or 'super-scale' with
439 cell volume (28, 38). Therefore, we suspect that regulators of formin activity may exhibit similar scaling
440 behaviors, so that their abundance scales with other aspects of cell geometry (e.g., cell length or cell
441 surface area). Alternatively, it has been recently demonstrated that cells can also exploit the different
442 rates at which cell volume and surface area scale to tune the size of their mitotic spindle and nucleus with
443 cell size (39, 40). Thus, it is possible that budding yeast utilize a similar mechanism to tune the activity of
444 formins in a cell length dependent manner.

445 Importantly, our new model of actin cable length control was inspired by studies investigating the actin
446 cytoskeleton arrays assembled by diverse cell types (e.g., *Listeria* and fish keratocyte lamellipodial
447 fragments) that observed similar actin density tapering profiles (25, 26). While these structures provide
448 fundamentally different biological functions (e.g., generating the force required for motility, or serving as
449 tracks for intracellular transport) it appears that much of their behavior is controlled through a simple set
450 of components – nucleators that promote the assembly of filaments, bundling or cross-linking factors that
451 organize filaments into a higher ordered network, and disassembly factors that prune filaments from
452 these arrays. While other studies have proposed that these diverse networks arise due to their association
453 with specific molecular regulators, our model suggests that these higher order actin arrays have much
454 more in common than previously thought. Furthermore, our work contributes to the emerging paradigm
455 that, in addition to molecular regulation, the dynamics and sizes of cytoskeletal networks are encoded by
456 their geometry (21, 41–43).

457 **References**

458 1. Y.-H. M. Chan, W. F. Marshall, How Cells Know the Size of Their Organelles. *Science* **337**, 1186–1189
459   (2012).

460 2. A. Haupt, N. Minc, How cells sense their own shape – mechanisms to probe cell geometry and their
461   implications in cellular organization and function. *J Cell Sci* **131**, jcs214015 (2018).

462 3. S. Reber, N. W. Goehring, Intracellular Scaling Mechanisms. *Cold Spring Harb Perspect Biol*, a019067
463   (2015).

464 4. L. Mohapatra, B. L. Goode, P. Jelenkovic, R. Phillips, J. Kondev, Design Principles of Length Control of
465   Cytoskeletal Structures. *Annu. Rev. Biophys.* **45**, 85–116 (2016).

466 5. N. W. Goehring, A. A. Hyman, Organelle Growth Control through Limiting Pools of Cytoplasmic
467   Components. *Current Biology* **22**, R330–R339 (2012).

468 6. G. Greenan, *et al.*, Centrosome Size Sets Mitotic Spindle Length in Caenorhabditis elegans Embryos.
469   *Current Biology* **20**, 353–358 (2010).

470 7. W. F. Marshall, H. Qin, M. R. Brenni, J. L. Rosenbaum, Flagellar Length Control System: Testing a Simple
471   Model Based on Intraflagellar Transport and Turnover. *MBoC* **16**, 270–278 (2005).

472 8. S. G. McInally, J. Kondev, S. C. Dawson, Length-dependent disassembly maintains four different
473   flagellar lengths in Giardia. *eLife* **8**, e48694 (2019).

474 9. L. Mohapatra, B. L. Goode, J. Kondev, Antenna Mechanism of Length Control of Actin Cables. *PLoS*
475   *Comput Biol* **11**, e1004160 (2015).

476 10. V. Varga, C. Leduc, V. Bormuth, S. Diez, J. Howard, Kinesin-8 Motors Act Cooperatively to Mediate
477   Length-Dependent Microtubule Depolymerization. *Cell* **138**, 1174–1183 (2009).

478 11. J. B. Moseley, B. L. Goode, The Yeast Actin Cytoskeleton: from Cellular Function to Biochemical
479   Mechanism. *MMBR* **70**, 605–645 (2006).

480 12. S. M. Buttery, S. Yoshida, D. Pellman, Yeast Formins Bni1 and Bnr1 Utilize Different Modes of Cortical
481   Interaction during the Assembly of Actin Cables□D □V. *In Vivo* **18**, 13 (2007).

482 13. M. Evangelista, D. Pruyne, D. C. Amberg, C. Boone, A. Bretscher, Formins direct Arp2/3-independent
483   actin filament assembly to polarize cell growth in yeast. *Nat Cell Biol* **4**, 32–41 (2002).

484 14. D. Pruyne, L. Gao, E. Bi, A. Bretscher, Stable and Dynamic Axes of Polarity Use Distinct Formin Isoforms
485   in Budding Yeast. *MBoC* **15**, 4971–4989 (2004).

486 15. A. Bretscher, Polarized growth and organelle segregation in yeast. *J Cell Biol* **160**, 811–816 (2003).

487 16. M. Chesarone, C. J. Gould, J. B. Moseley, B. L. Goode, Displacement of Formins from Growing Barbed
488   Ends by Bud14 Is Critical for Actin Cable Architecture and Function. *Developmental Cell* **16**, 292–302
489   (2009).

490 17. M. Chesarone-Cataldo, *et al.*, The Myosin Passenger Protein Smy1 Controls Actin Cable Structure and
491   Dynamics by Acting as a Formin Damper. *Developmental Cell* **21**, 217–230 (2011).

492 18. J. A. Eskin, A. Rankova, A. B. Johnston, S. L. Alioto, B. L. Goode, Common formin-regulating sequences
493   in Smy1 and Bud14 are required for the control of actin cable assembly in vivo. *MBoC* **27**, 828–837
494   (2016).

495 19. S. G. McInally, J. Kondev, B. L. Goode, Scaling of subcellular actin structures with cell length through
496   decelerated growth. *eLife* **10**, e68424 (2021).

497 20. T. Kamasaki, R. Arai, M. Osumi, I. Mabuchi, Directionality of F-actin cables changes during the fission
498   yeast cell cycle. *Nat Cell Biol* **7**, 916–917 (2005).

499 21. A. Manhart, *et al.*, Quantitative regulation of the dynamic steady state of actin networks. *eLife* **8**,
500   e42413 (2019).

501 22. P. J. Michalski, A. E. Carlsson, A model actin comet tail disassembling by severing. *Phys. Biol.* **8**, 046003
502   (2011).

503 23. P. J. Michalski, A. E. Carlsson, The effects of filament aging and annealing on a model lamellipodium
504   undergoing disassembly by severing. *Phys. Biol.* **7**, 026004 (2010).

505 24. H. Y. Kueh, W. M. Brieher, T. J. Mitchison, Quantitative Analysis of Actin Turnover in Listeria Comet
506   Tails: Evidence for Catastrophic Filament Turnover. *Biophysical Journal* **99**, 2153–2162 (2010).

507 25. N. Ofer, A. Mogilner, K. Keren, Actin disassembly clock determines shape and speed of lamellipodial
508   fragments. *Proceedings of the National Academy of Sciences* **108**, 20394–20399 (2011).

509 26. J. A. Theriot, T. J. Mitchison, L. G. Tilney, D. A. Portnoy, The rate of actin-based motility of intracellular
510   Listeria monocytogenes equals the rate of actin polymerization. *Nature* **357**, 257–260 (1992).

511 27. C. A. H. Allard, F. Decker, O. D. Weiner, J. E. Toettcher, B. R. Graziano, A size-invariant bud-duration
512   timer enables robustness in yeast cell size control. *PLoS ONE* **13**, e0209301 (2018).

513 28. G. E. Neurohr, *et al.*, Excessive Cell Growth Causes Cytoplasm Dilution And Contributes to Senescence.
514   *Cell* **176**, 1083-1097.e18 (2019).

515 29. P. Jorgensen, Systematic Identification of Pathways That Couple Cell Growth and Division in Yeast.
516   *Science* **297**, 395–400 (2002).

517 30. S. M. Buttery, K. Kono, E. Stokasimov, D. Pellman, Regulation of the formin Bnr1 by septins anda
518   MARK/Par1-family septin-associated kinase. *MBoC* **23**, 4041–4053 (2012).

519 31. L. Gao, W. Liu, A. Bretscher, The Yeast Formin Bnr1p Has Two Localization Regions That Show Spatially
520   and Temporally Distinct Association with Septin Structures. *MBoC* **21**, 1253–1262 (2010).

521 32. M. V. Garabedian, *et al.*, A septin-Hof1 scaffold at the yeast bud neck binds and organizes actin cables.
522   *MBoC*, mbc.E19-12-0693 (2020).

523 33. I. V. Kukhtevich, N. Lohrberg, F. Padovani, R. Schneider, K. M. Schmoller, Cell size sets the diameter of
524   the budding yeast contractile ring. *Nat Commun* **11**, 2952 (2020).

525 34. I. Soifer, L. Robert, A. Amir, Single-Cell Analysis of Growth in Budding Yeast and Bacteria Reveals a
526   Common Size Regulation Strategy. *Current Biology* **26**, 356–361 (2016).

527 35. M. V. Garabedian, *et al.*, Integrated control of formin-mediated actin assembly by a stationary
528   inhibitor and a mobile activator. *Journal of Cell Biology* **217**, 3512–3530 (2018).

529 36. B. R. Graziano, *et al.*, The F-BAR protein Hof1 tunes formin activity to sculpt actin cables during
530   polarized growth. *Mol Biol Cell* **25**, 1730–1743 (2014).

531 37. L. M. F. de Godoy, *et al.*, Comprehensive mass-spectrometry-based proteome quantification of
532   haploid versus diploid yeast. *Nature* **455**, 1251–1254 (2008).

533 38. M. C. Lanz, *et al.*, Increasing cell size remodels the proteome and promotes senescence. *Molecular
534   Cell* **82**, 3255-3269.e8 (2022).

535 39. C. Brownlee, R. Heald, Importin α Partitioning to the Plasma Membrane Regulates Intracellular
536   Scaling. *Cell* **176**, 805-815.e8 (2019).

537 40. E. Rieckhoff, *et al.*, Spindle scaling is governed by cell boundary regulation of microtubule nucleation
538   (2020) https:/doi.org/10.1016/j.cub.2020.10.093 (June 16, 2020).

539 41. R. M. Garner, J. A. Theriot, Leading edge maintenance in migrating cells is an emergent property of
540   branched actin network growth. *eLife* **11**, e74389 (2022).

541 42. A.-C. Reymann, *et al.*, Nucleation geometry governs ordered actin networks structures. *Nature Mater*
542   **9**, 827–832 (2010).

543 43. A. Rosario, S. G. McInally, P. R. Jelenkovic, B. L. Goode, J. Kondev, Universal length fluctuations of actin
544   structures found in cells. 2023.07.27.550898 (2023).

545 44. S. McInally, J. Kondev, B. Goode, Quantitative Analysis of Actin Cable Length in Yeast. *BIO-PROTOCOL*
546   **12** (2022).

547

Methods:

Plasmids and yeast strains

All strains (see Supplemental Table 1) were constructed using standard methods. To integrate the GFP variant (Envy) at the C-terminus of the endogenous Bnr1, primers were designed with complementarity to the 3' end of the GFP^{Envy} cassette and the C-terminal coding region of Bnr1. PCR was used to generate amplicons from the pFA6a-GFP-His3MX template that allow for selection of transformants using media lacking histidine. The parent strain, *cdc28-13^{ts}*, was transformed with PCR products, and transformants were selected by growth on synthetic media lacking histidine. To integrate a mCherry tag at the C-terminus of the endogenous Cdc3, the plasmid pBG1533 (Cdc3-mCherry-LEU) was linearized using the restriction enzyme BglII and transformed into the parent strain, *cdc28-13^{ts}; Bnr1-GFP^{Envy}::His3MX*. Transformants were selected by growth on synthetic media lacking leucine.

Induction of cell size changes

To induce increases in cell size, *cdc28-13^{ts}* cells were grown at the permissive temperature (25°C) overnight in synthetic complete media (SCM), then 10 μL of overnight culture was diluted into 5mL of fresh SCM. Cultures were then shifted to the restrictive temperature (37°C) for either 4 or 8 hours. After this induction, cells were returned to the permissive temperature (25°C) for one hour of growth to allow cell polarization and bud growth, and then used for imaging experiments.

Quantitative analysis of actin cable length, number, and fluorescence intensity in fixed cells

Strains were grown at 25°C to mid-log phase (OD600 ~ 0.3) in synthetic complete media (SCM) or were first induced for cell size changes as indicated above. Then cells were fixed in 4.4% formaldehyde for 45 minutes, washed three times in phosphate-buffered saline (1XPBS), and stained with Alexa Fluor 488-phalloidin (Life Technologies) for ≥24 hours at 4°C. Next, cells were washed three times in 1XPBS and imaged in Vectashield mounting media (Vector Laboratories). 3D stacks were collected at 0.2 μm intervals on either a Zeiss LSM 880 using Airyscan super-resolution imaging equipped with 63× 1.4 Plan-Apochromat Oil objective lens, or a Nikon Ti2-E invert confocal microscope equipped with a CSU-W1 SoRa (Yokogawa) and a Prime BSI sCMOS camera (Teledyne Photometrics) controlled by Nikon NIS-Elements Advanced Research software using a 100x, 1.45 NA objective. 3D stacks were acquired for the entire height of the cell. Airyscan image processing was performed using Zen Black software (Carl Zeiss) and SoRa image processing was performed using NIS-Elements Advanced Research software (Nikon). Quantification of actin cable length was performed as previously described (44).

To quantify actin cable number, we generated line scans of phalloidin fluorescence intensity across the approximate equator of the mother cell from background subtracted maximum intensity projection images. Lines were drawn to avoid fluorescence signal intensity associated with actin patches. Actin cables were counted by automated detection of fluorescence peaks from line scan profiles using custom Python

589 scripts. Peaks were only identified as cables if their fluorescence intensity was greater than 20% of the
590 maximum peak intensity within a single line scan.

591 To quantify the fluorescence intensity along the length of cables, we manually traced individual cables in
592 background subtracted sum intensity projection images, from the bud neck to their terminus in the
593 mother cell. We only included clearly discernable cables that did not intersect with other cables or actin
594 patches. We used these line scans to record the fluorescence intensity at each position along the cable.
595 To compare the fluorescence decay profiles of cables from different cells, the data were imported into
596 custom Python scripts where their fluorescence intensity was normalized and rescaled so that the
597 maximum intensity was equal to one, and the minimum fluorescence value was set to zero. These profiles
598 were fit to a single exponential to measure their decay length.

Simulation protocol

600 We used stochastic simulations to simulate the assembly of actin cables based on our two-dimensional
601 model of cable length control. In the simulation, the system is composed of a number of rows (determined
602 by the number of formins, N_f, contributing to cable assembly) in which filaments of length L_f are added.
603 We start these simulations with a row that contains zero filaments (i.e., a single formin that has not
604 assembled any actin filaments) and then follow the trajectory of this row over time. For each step of the
605 simulation, a single filament of length L_f is added to the row, and all other filaments within that row are
606 selected to undergo one of the possible transitions – they are removed from the row or they remain in
607 the row. These transitions are chosen at random based on their relative weight, which is proportional to
608 the rate of the transition. Following these transitions, the system is updated to a new state and another
609 step of the simulation is executed. The time elapsed between simulation steps is determined by the time
610 required for a filament of length L_f to be assembled by the formin at the assembly rate, k_+. This process is
611 independently repeated for each row of the system, based on the number of formins (N_f), and the length
612 of the entire cable is determined as the distance from the initial filament position in the row to the distal
613 end of the longest surviving filament in any row. This process is repeated for long enough time such that
614 the length of the cable reaches steady state.

Quantification of Bnr1 bud neck fluorescence intensity

616 Strains were first induced for cell size changes as indicated above and the density of each culture was
617 measured using a spectrophotometer. The density of each culture was normalized by adding additional
618 synthetic complete media (SCM) to the culture tube, and equal amounts of cells were harvested by
619 centrifugation. Media was decanted and cells were resuspended in 50 µL fresh SCM and combined into a
620 single tube and gently mixed. Approximately 5 µL of the cell suspension mixture was added onto a 1.2%
621 agarose pad (made with SCM), and 3D stacks were collected at 0.2 µm intervals were acquired at room
622 temperature on a Marianas spinning disk confocal system (3I, Inc, Denver,CO), consisting of a Zeiss
623 Observer Z1 microscope equipped with a Yokagawa CSU-X1 spinning disk confocal head, a QuantEM
624 512SC EMCCD camera, PLAN APOCHROMAT 100X oil immersion objectives (NA 1.4) and Slidebook
625 software. Images were processed using custom ImageJ macros. Briefly, sum intensity projections were
626 generated and the Cdc3-mCherry channel was used for segmentation of the bud neck region of each cell.
627 These segmentation masks were used to the measure the total fluorescence intensity of Bnr1-GFP[Envy] for
628 each cell and the lengths of each cell (i.e., the distance from the bud neck to the rear of the cell) were
629 manually measured.

Data and materials availability:

631 Data are available in the main text or in the supplementary material. All images are archived at Zenodo
632 and source code is available at GitHub (https://github.com/shanemc11/2DCableModel).

633 **Supplemental text: Two dimensional model of cable assembly**

634 To describe the dynamics of cable assembly we consider a model which describes an actin cable as a
635 composite structure made of actin filaments cross-linked into a bundle; see Figure 1C. Assembly of the
636 cable proceeds at multiple formin molecules (N_f) localized at the bud neck. We assume that each formin
637 produces an actin filament of a fixed length (L_f) which is incorporated into the growing actin cable at a
638 constant rate (k_+). These filaments are bundled together by crosslinkers and as a result the entire cable
639 collectively treadmills as a single unit, extending into the mother cell at a constant extension velocity
640 ($v_{extension} = k_+ L_f$). In the model we describe this two-dimensional cable structure as consisting of N_f
641 lanes, as shown in Figure 1C.

642 Once incorporated into the growing bundle, each filament has an independent probability of being
643 targeted for removal by the action of disassembly factors. We assume that the filaments are removed at
644 a rate k_- which makes the geometry of a cable tapered, with different lanes at any given point in time
645 having a different length. The combined action of filament addition and removal from the N_f lanes leads
646 to cable-length dynamics, where the cable length (L_c) is defined as the length of the longest lane.

647 Our goal is to compute the dynamics and steady state properties of the cable length. Specifically, below
648 we compute the probability distribution of cable lengths, its mean and variance, the steady state tapered
649 profile of the cable, as well as the time evolution of the average cable-length, for cables that start with
650 zero length. All these quantities we measure in our single cell experiments and, as described in the main
651 text, we use these measurements to test our model.

652   1. Steady state cable length distribution

653 To compute the steady state cable length we use ideas from extreme value statistics pioneered by Fisher.
654 To compute the probability distribution of cable lengths we consider the probability that the cable length
655 is less than L:

656
$$p_{N_f}(L_C < L) = p_1(L_1 < L)^{N_f} \qquad\qquad S.1$$

657 where $p_1(L_1 < L)$ is the probability that the length L_1 of one lane of the cable is less than L. This formula
658 simply states that for the cable length to be less than some length L, then all the lanes must have a length
659 that is smaller than L. The additional assumption of our model is that each lane has dynamics that are
660 independent of every other lane, where filaments are added and removed to the lane independently of
661 what happens to filaments in the other lanes.

662 To compute $p_1(L_1 < L)$ we note that for a lane to have a length less than a specified length, the last
663 filament in that lane must be at a distance x less than L from the formin that made it. The probability of
664 that occurring is simply the probability that all the filaments at larger distances have been removed by the
665 action of the disassembly factors, i.e.,

666
$$p_1(L_1 < L) = \prod_{i=\frac{L}{L_f}}^{\infty} (1 - e^{-k_- \tau_i}) \qquad\qquad S.2$$

667 Here $\tau_i \equiv \dfrac{i\,L_f}{v_{extension}}$ is the time that it takes the i$^{\text{th}}$ filament to arrive at a distance iL_f from the formin by
668 virtue of the whole cable structure extending at a constant speed $v_{extension}$. The expression $1 - e^{-k_- \tau_i}$ is
669 simply the probability that by time τ_i the i$^{\text{th}}$ filament has been removed from the cable by disassembly
670 factors, which remove filaments at rate k_-.

671 Using the approximation $(1 - \epsilon) \approx e^{-\epsilon}$ for small ϵ, we can rewrite equation S.2 as

672
$$p_1(L_1 < L) = e^{-\sum_{i=\frac{L}{L_f}}^{\infty} \frac{L}{L_f} \exp\left(-\frac{k_- L_f}{v_{extension}} i\right)}$$

673 which after approximating the sum with an integral over $x \equiv L_f\, i$ gives the formula

674
$$p_1(L_1 < L) = e^{-\frac{v_{extension}}{k_- L_f} e^{-\frac{k_- L}{v_{extension}}}}. \qquad S.3$$

675

676 Replacing this result into equation S.1 leads to the cumulative distribution of cable lengths, when the
677 cable consists of N_f lanes:

678
$$p_{N_f}(L_C < L) = e^{-N_f \frac{\lambda}{L_f} e^{-\frac{L}{\lambda}}} \qquad S.4$$

679 where we have introduced the characteristic length scale $\lambda \equiv \frac{v_{extension}}{k_-}$ which is the average distance over
680 which a filament is transported by the extending cable during its lifetime, which on average is $\frac{1}{k_-}$. The
681 derivative of the cumulative distribution with respect to L yields the probability density function, which is
682 in good agreement with stochastic simulations of the model (Supplemental Figure 2B).

683 Using $N_f \frac{\lambda}{L_f} = e^{\ln\left(N_f \frac{\lambda}{L_f}\right)}$ we can rewrite equation S.4 as

684
$$p_{N_f}(L_C < L) = e^{-e^{-\frac{L - \lambda \ln(N_f \lambda / L_f)}{\lambda}}} = e^{-e^{-\frac{L-\mu}{\beta}}} \qquad S.5$$

685 which is the Gumbel distribution with location parameter $\mu = \lambda \ln(N_f \lambda / L_f)$ and scale parameter $\beta = $
686 λ. The mean of the Gumbel distribution is $\mu + \beta\gamma$ ($\gamma = 0.5772 \ldots$ is the Euler-Mascheroni constant), while
687 the variance is $\frac{\pi^2}{6}\beta^2$. In our case, this leads to the formulas for the mean and variance of the cable length:

688
$$\langle L \rangle = \lambda\left(\ln\left(N_f \lambda / L_f\right) + \gamma\right) \qquad S.6$$

689 and

690
$$Var(L) = \frac{\pi^2}{6}\lambda^2. \qquad S.7$$

691

692 Replacing $\lambda = k_+ L_f / k_-$ into the formulas for the mean and the variance,

693
$$\langle L \rangle = L_f \frac{k_+}{k_-}\left(\ln\left(N_f k_+ / k_-\right) + \gamma\right) \qquad S.8$$

694
$$Var(L) = \frac{\pi^2}{6}\left(\frac{k_+}{k_-}\right)^2 L_f^2 \qquad S.9$$

695 we arrive at an important result, namely that if changes in cable length are affected by changing the length
696 of the individual filaments while keeping the number of formins and the rates of adding and removing the
697 filaments from the cable constant, then the variance will scale as the square of the mean cable length.
698 This is scaling we observe when changing the length of the cell, and this implies that the length of the
699 filaments in the cable must scale with the length of the cell. This is a sharp prediction of our model that
700 could be tested by taking EM images of cables in differently sized yeast cells.

701

702   2. Time evolution of the cable length

703 Using the model of cable assembly described above we can compute the time evolution of the average
704 cable length, assuming that at zero time the length of the cable is zero. In experiments we obtain this
705 quantity by watching fluorescently labeled cables extend from the bud neck to the rear of the yeast cell.

706 To compute the average cable length as a function of time, we start by computing the probability for the
707 cable being shorter than some length $(L_c < L)$ if time t has elapsed from the moment the cable started
708 extending from the formins at the bud neck:

709
$$p_{N_f}(L_c < L, t) = \left[\prod_{i=L/L\_f}^{v_{extension}\, t/L_f} \left(1 - e^{-\frac{k_-\, L_f}{v_{extension}}\, i} \right) \right]^{N_f}. \qquad S.10$$

710 This formula assumes that the length of the cable L is smaller than the largest possible distance $v_t t$ that
711 a filament can be found away from the formin, given that it has been advected with treadmilling speed
712 v_t over time t; for larger lengths the probability is zero. The idea behind this formula is that for a cable to
713 have a length less than L, then all the lanes have to be devoid of filaments that are at distances greater
714 than L from the bud neck (where the formins, which inject the filaments into the cable, reside). The
715 formula $1 - e^{-\frac{k_-\, L_f}{v_{extension}}\, i}$ gives the probability that the filament at distance $L_f i$ (i is an integer that counts
716 filaments from the bud neck) has been disassembled, given that the rate of disassembly is k_-;
717 $L_f i / v_{extension}$ is the time that filament has been in the cable since it was injected at the bud neck by the
718 action of a formin.

719 Using the same approximation as in the calculation above for the steady state distribution, we can simplify
720 equation S.10 to

721
$$p_{N_f}(L_c < L, t) = e^{-N_f\, \frac{\lambda}{L_f}\left[e^{-\frac{L}{\lambda}} - e^{-k_- t} \right]}. \qquad S11$$

722 where, as above, we introduce the characteristic length scale $\lambda \equiv \frac{v_{extension}}{k_-}$, which is the average distance
723 over which a filament is transported by the treadmilling action of the cable during its lifetime.

724 From the cumulative distribution, equation S.11, we can compute the mean cable length at time t as an
725 integral

726
$$\langle L \rangle(t) = \int_0^{\lambda k_- t} (1 - p_{N_f}(L_c < L, t))\, dL$$

727 which comes out to be

728
$$\langle L \rangle(t) \approx \lambda \left[k_- t - e^{N_f \frac{\lambda}{L_f} e^{-k_- t}} \left(E_i \left(-N_f \frac{\lambda}{L_f} \right) - E_i \left(-N_f \frac{\lambda}{L_f} e^{-k_- t} \right) \right) \right] \qquad S.12$$

729 Where $E_i(x)$ is the exponential integral function. As shown in Supplemental Figure 2C in the main text
730 this formula is in excellent agreement with stochastic simulations of the treadmilling model.

731   3. Tapering of the cable profile

732 Within our model we define the width of the cable $W(x)$ as the expected number of filaments present at
733 distance x away from the bud neck. Given that each cable starts out with a width that is set by the number
734 of formins N_f, $W(0) = N_f$, the average number of filaments at distance x, is given by the survival
735 probability that the filament was not disassembled over the time $\tau = x/v_{extension}$, where $v_{extension}$ is
736 the treadmilling speed of the filaments in the cable. Given that the rate of removal of filaments from the
737 cable is k_-, we find

738
$$W(x) = N_f \, p(x) = N_f e^{-k_- \tau} = N_f e^{-k_- \frac{x}{v_{extension}}} = N_f \, e^{-\frac{x}{\lambda}}.$$

739 The prediction of our model is that the cable width decays exponentially with the distance away from the
740 bud neck, which is what we observe experimentally. The decay length is set by the characteristic length
741 λ.

742

743 **Figure legends:**

744 **Figure 1:** Two-dimensional model of cable length control. (A) Representative maximum intensity
745 projection images of haploid yeast cells fixed and stained with labeled-phalloidin. Arrows indicate single
746 actin cables that clearly display their tapered shape. Scale bar, 5µm. (B) Relative actin cable fluorescence
747 intensity measured in three independent experiments. Solid magenta line and shading, mean and 95%
748 confidence interval for all three experiments (n=47 cables). Tapering profile decay length (±95% CI) was
749 determined by fitting the profile to a single exponential. (C) Schematic of the two-dimensional model of
750 actin cable length control. Multiple formins (orange, N_f) simultaneously assemble short actin filaments
751 with a characteristic length (L_f) at a constant rate (k_+). These filaments are crosslinked and bundled
752 (green ellipses) with neighboring filaments to form the cable and continue to extend into the cell at the
753 same rate at which filaments are assembled by formins ($v_{extension} = k_+ L_f$). Each filament has an
754 independent probability of being targeted for removal ($r_{disassemble} = k_- L_f$) from the cable. Thus, the
755 length of the cable (L_c) is the distance from the site of assembly to the distal tip of the longest surviving
756 filament in the cable. (D-F) Results obtained from simulations (solid black lines) compared with
757 experimental measurements of cable length (D), cable extension rate (E), and cable tapering (F). The
758 parameters used for these 1,000 independent simulations were, k_+ = 0.50 sec⁻¹, k_-= 0.16 sec⁻¹, L_f =
759 500nm, N_f = 4 formins. Solid lines and shading indicate mean and 95% confidence interval, respectively.

760 **Figure 2:** The amount of Bnr1 formin at the bud neck and the number of actin cables in a cell scale with
761 cell length. (A) Representative maximum intensity projection image of *cdc28-13ts* cells grown to different
762 sizes while expressing fluorescently labeled Bnr1 (Bnr1-GFP[Envy]) and Cdc3 (Cdc3-mCherry). Scale bar, 5µm.
763 (B) Amount of Bnr1-GFP[Envy] localized to the bud neck of *cdc28-13ts* cells grown to different sizes plotted
764 against mother cell length on a double logarithmic plot and fit using the power-law. Bnr1-GFP[Envy] was
765 measured in three independent experiments (n=148 cells). (C) Representative maximum intensity
766 projection images of a haploid yeast cell fixed and stained with labeled-phalloidin. Scale bar, 2µm. Yellow
767 bar indicates the ROI position used to generate the line scan profile (D) used for automated peak detection

768   (orange X's indicate detected actin cables). (E) The number of actin cables measured from haploid (red),
769   diploid (blue), uninduced *cdc28-13^{ts}* (green), and induced *cdc28-13^{ts}* (yellow) cells fixed and stained with
770   labeled-phalloidin. Each data point represents an individual cell. Larger symbols represent the mean from
771   each of the three independent experiments (n=119 cells). Error bars indicate 95% confidence intervals.
772   Statistical significance determined by students t-test. Significant differences (p≤0.05) indicated for
773   comparisons with haploid ('a'), diploid ('b'), uninduced cdc28-13ts ('c'), and induced cdc28-13ts ('d'). (F)
774   Actin cable number plotted against mother cell length on a double logarithmic plot and fit using the
775   power-law.

776   **Figure 3:** Actin cable tapering is cell length dependent. (A) Representative maximum intensity projection
777   images of small (left) and large (right) *cdc28-13^{ts}* cells fixed and stained with labeled-phalloidin. Arrows
778   indicate single actin cables that clearly display their tapered shape. Scale bar, 5µm. (B) Actin cable length
779   and (C) actin cable fluorescence intensity in the bud neck region measured from mixed populations of
780   uninduced and induced *cdc28-13^{ts}* cells. Cells were binned based on cell length (E), small cells are indicated
781   in green while large cells are indicated in yellow. Each data point represents an individual cable. Larger
782   symbols represent the mean from each experiment. Error bars indicate 95% confidence intervals.
783   Statistical significance determined by students t-test. (D) Relative actin cable fluorescence intensity
784   plotted against cable length, and (F) relative actin cable fluorescence intensity plotted against the ratio of
785   cable length/cell length. Solid lines and shading, mean and 95% confidence interval. Tapering profile decay
786   lengths (±95% CI) were determined by fitting each profile to a single exponential. All data were generated
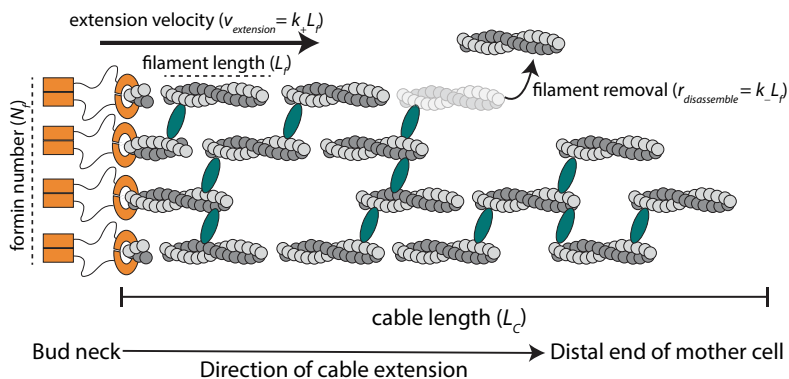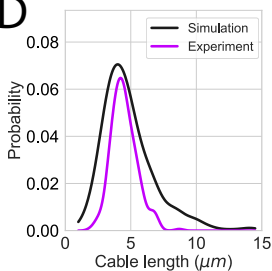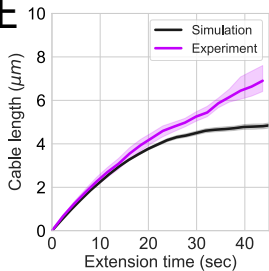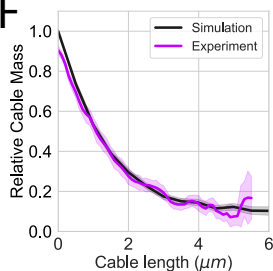787   from five independent experiments (n=84 cables).

788   **Figure 4:** Tuning the length of formin generated filaments scales actin cable length with cell length. (A) (B-
789   E) Comparisons between simulations conducted using the cell size specific filament lengths (black and
790   grey lines) with experimentally measured actin cable parameters from uninduced (green lines) and
791   induced *cdc28-13^{ts}* cells (yellow lines). (B-C) Comparisons of actin cable length distributions, (D) actin cable
792   tapering profiles, and (E) actin cable extension rate. Solid lines and shading indicate mean and 95%
793   confidence intervals, respectively.

794   **Supplemental Figure 1:** Cable extension velocity is independent of cell size. (A) Actin cable length plotted
795   against cable extension time measured in five independent experiments (n= 82 cables). Cable extension
796   velocity (±95%CI) (black, dashed line) was determined by linear regression using the first ~10 seconds of
797   extension. Symbols at each time point represent the mean for individual experiment. Solid lines and
798   shading, mean and 95% confidence interval for all five experiments. (B) Cable extension rates for
799   uninduced (green line) and induced *cdc28-13^{ts}* (yellow line) cells, from at least three independent
800   experiments (≥57 cables/strain). Cable extension velocity (±95%CI) in uninduced (black, dashed line) and
801   induced *cdc28-13^{ts}* (grey, solid line) cells was determined by linear regression using the first ~10 seconds
802   of extension. Solid and shading, mean and 95% confidence intervals for all experiments.

803   **Supplemental Figure 2:** (A) Tiled heat map displaying predicted mean actin cable lengths where the
804   number of formins and filament lengths are varied. Each tile represents the mean cable length (indicated
805   on face of each tile) from a unique combination of formin number and filament length while λ is held
806   constant. Divergent color coding indicates mean cable lengths that are longer (green shading) or shorter
807   (purple shading) than mean length along the diagonal (white, $< L_c > = 4.3$ µm). (B-D) Results obtained
808   from simulations (solid black lines) and analytical solutions (dashed red lines) show that the two-
809   dimensional model of cable length control model produces a peaked distribution of cable lengths (A),
810   decelerating cable extension rates (B), and cables with a tapered shape (C). The parameters used for these
811   1,000 independent simulations were, k_+ = 0.50 sec^{-1}, k_-= 0.16 sec^{-1}, L_f = 500nm, N_f = 4 formins. Solid
812   lines and shading indicate mean and 95% confidence interval, respectively.

813   **Supplemental Figure 3:** (A-D) Comparisons between simulations conducted using the cell size specific
814   disassembly rates (black and grey lines) with experimentally measured actin cable parameters from
815   uninduced (green lines) and induced *cdc28-13^{ts}* cells (yellow lines). (A) Comparisons of actin cable tapering
816   profiles, (B-C) actin cable length distributions, and (D) actin cable extension rate. Solid lines and shading
817   indicate mean and 95% confidence interval, respectively.

818   **Supplemental table 1:** Yeast strains used in this study. The genotype, source, and related data are
819   indicated for each strain used in this study.

Figure 1: Two-dimensional model of cable length control.
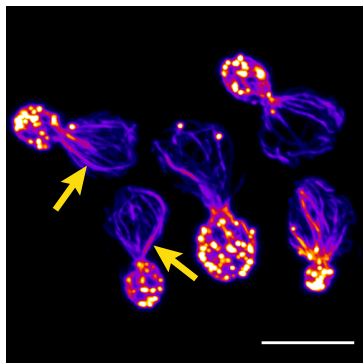
A

B
Decay length = 1.54±0.08, R^2 = 0.89
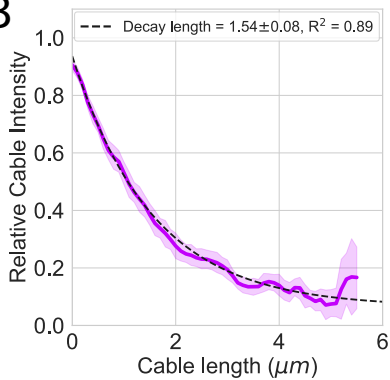
Relative Cable Intensity

Cable length (μm)

C
extension velocity ($v_{extension} = k_+ L_f$)

filament length (L_f)

filament removal ($r_{disassemble} = k_- L_f$)

formin number (N)

cable length (L_c)

Bud neck → Direction of cable extension → Distal end of mother cell

D
Simulation
Experiment

Probability

Cable length (μm)

E
Simulation
Experiment

Cable length (μm)

Extension time (sec)

F
Simulation
Experiment

Relative Cable Mass

Cable length (μm)

Figure 2: The amount of Bnr1 formin at the bud neck and the number of actin cables in a cell scale with cell length.
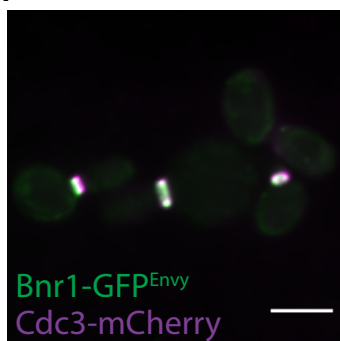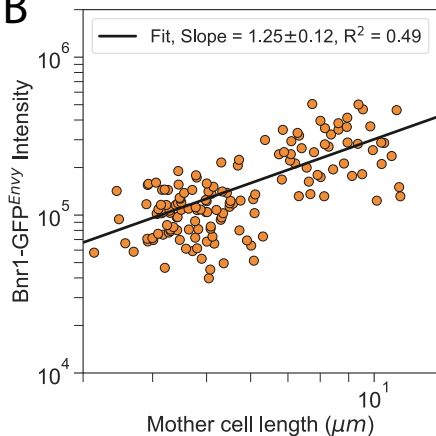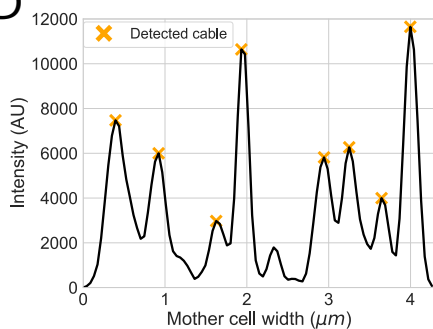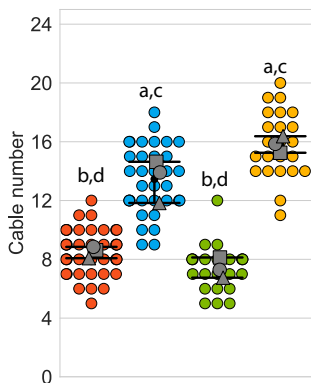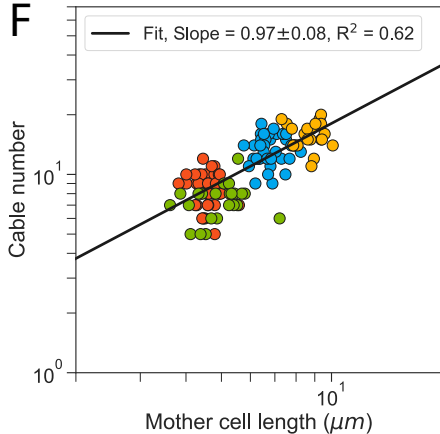
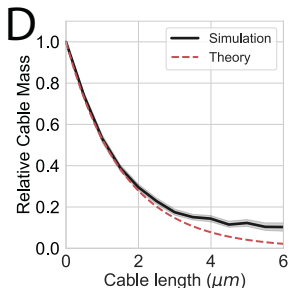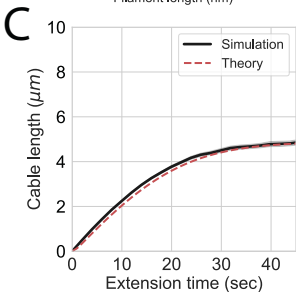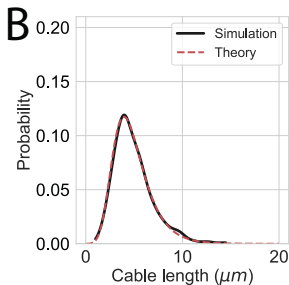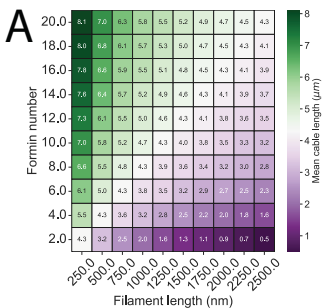**Figure 3: Actin cable tapering is cell length dependent.**
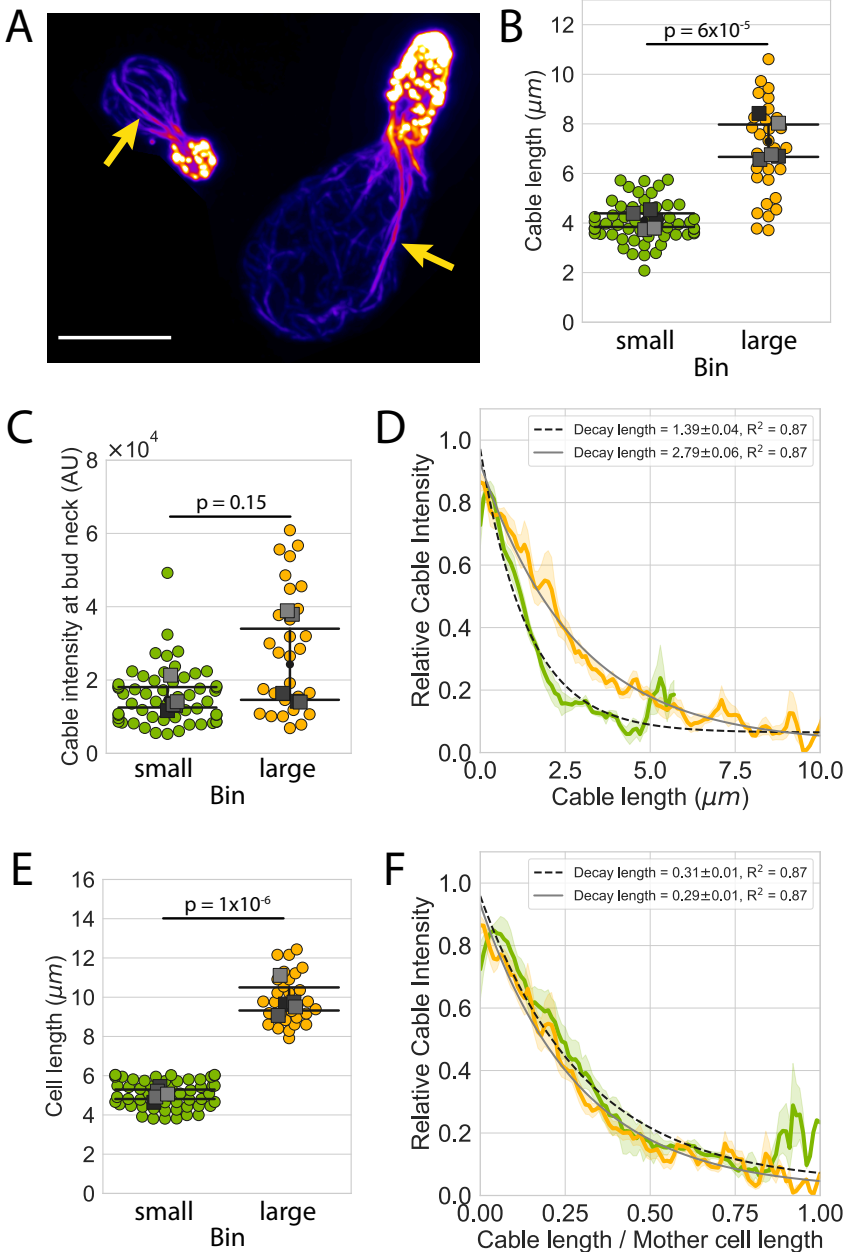
Figure 4: Tuning the length of formin generated filaments scales actin cable length with cell length.
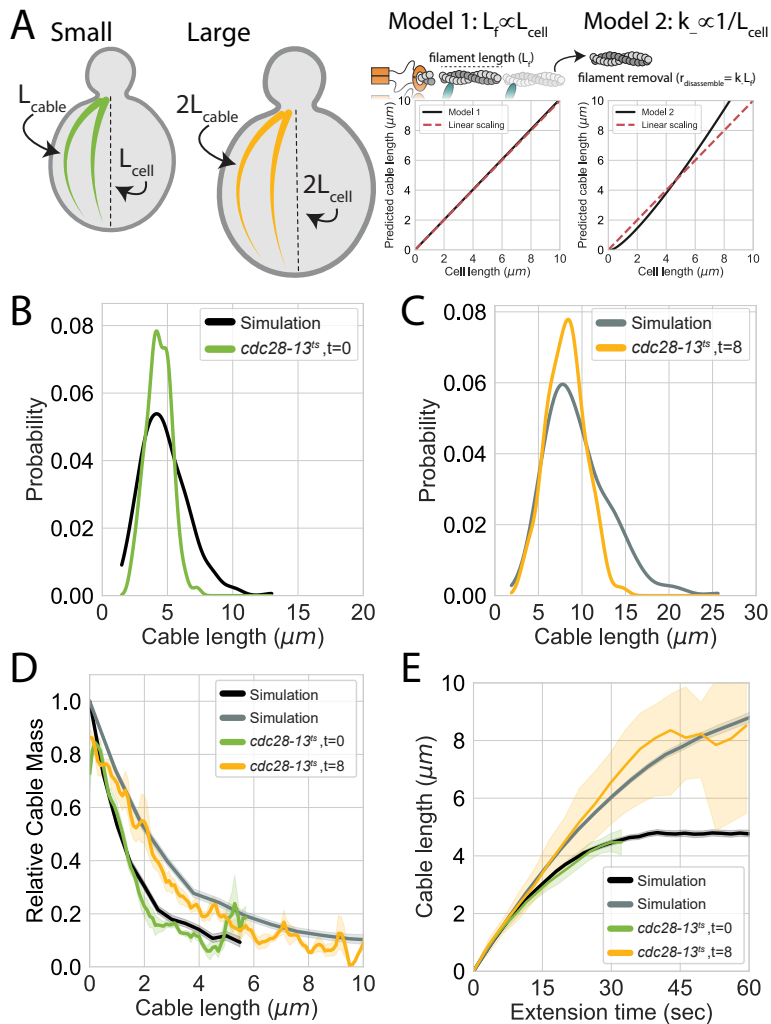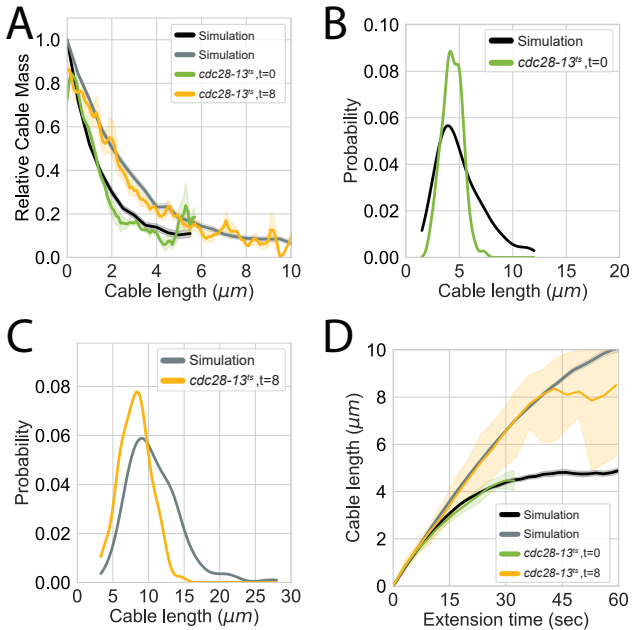
Supplemental Figure 1: Cable extension velocity is independent of cell size.
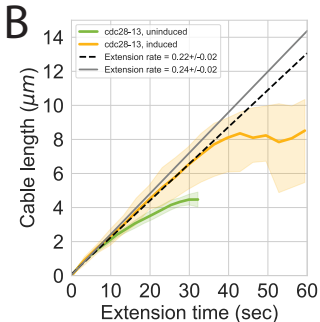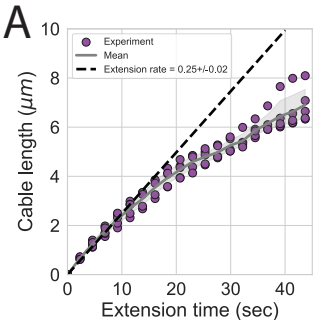
Supplemental Figure 2

Supplemental Figure 3

Supplementary table 1

Genotype	Source	Figures used in
his3-11,15;ura3-52;leu2-3,112;ade2-1;trp1-1;psi+;ssd-;GAL+	Lab stock	Fig. 1A-B, Fig. 1D,
his3-11,15/his3-11,15;ura3-52/ura3-52;leu2-3,112/leu2-3,112;ade2-1/ade2-1;trp1-1/trp1-1;psi+;ssd-;GAL+	Lab stock	Fig. 1F, Fig. 2C-F
	Lab stock	Fig. 2E-F
cdc28-13; his3-11,15 trp1-1 leu2-3 ura3-1 ade2-1	Lab stock	Fig. 2E-F, Fig. 3A-F, Fig. 4A-C, SFig. 4A-C
Abp140-Envy::SpHIS5; his3-11,15;ura3-52;leu2-3,112;ade2-1;trp1-1;psi+;ssd-;GAL+	Lab stock	Fig. 1E, SFig. 3A Fig. 4D, SFig. 3B,
cdc28-13; Abp140-Envy::SpHIS5; his3-11,15 trp1-1 leu2-3 ura3-1 ade2-1	Lab stock	SFig. 4D
cdc28-13; Bnr1-Envy::SpHIS5; Cdc3-mCherry::LEU2; his3-11,15 trp1-1 leu2-3 ura3-1 ade2-1	This study	Fig. 3A-B